State-of-Charge Estimation of Nickel–Cadmium Batteries Based on Dynamic Modeling of Electrical Characteristics and Adaptive Untrace Kalman Filtering

Meng Meng [1], Yiguo He [2], Yin Zhang [1], Haitao Liao [2] and Chaohua Dai [2,*]

[1] CRRC Qingdao Sifang Co., Ltd., Qingdao 266111, China; mengmeng@cqsf.com (M.M.); zhangyin@cqsf.com (Y.Z.)

[2] School of Electrical Engineering, Southwest Jiaotong University, Chengdu 610031, China; swjtuerheyiguo@163.com (Y.H.); liaohaitao2022@163.com (H.L.)

*   Correspondence: daichaohua@swjtu.edu.cn

Abstract: With the increasing demand for intelligence and automation, and the continuous strengthening of safety and efficiency requirements, the disadvantages of traditional "blind use" of nickel–cadmium batteries have become increasingly prominent, and the lack of state-of-charge (SOC) estimation needs to be changed urgently. For this purpose, a dynamic model of nickel–cadmium battery is established, and an SOC estimation method of nickel–cadmium battery based on adaptive untraced Kalman filter is proposed. Firstly, the experimental platform was built, and the open-circuit voltage and polarization characteristics of nickel–cadmium batteries were analyzed. On this basis, an equivalent circuit model is constructed to reflect the characteristics of nickel–cadmium batteries, and the model parameters were identified by the hybrid pulse power characteristic test; Then, based on the dynamic model, the SOC of the nickel–cadmium battery was estimated by combining with the Sage–Husa adaptive untrace Kalman filtering algorithm. Finally, the SOC estimation effect was verified under two operating conditions: Hybrid pulse power characteristic (HPPC) and constant cyclic charging and discharging power. The experimental results show that the proposed estimation method is insensitive to the initial value of SOC, and can still converge to the real value even if there is 30% error in the initial value. The mean absolute error and root mean square deviation of the final SOC estimation results are both less than 1%. The dynamic model and the proposed SOC estimation method provide valuable reference for the operation control, maintenance, and replacement of nickel–cadmium batteries in the use process.

Keywords: nickel–cadmium battery; state-of-charge estimation; equivalent circuit model; parameter identification; adaptive untraced Kalman filter; experimental verification

1. Introduction

With the increasing popularity of electric/hybrid transportation vehicles, the storage and utilization of energy is an important topic, especially regarding secondary batteries. Among them, the lithium-ion battery has emerged as a leading mobile energy storage solution for its remarkable characteristics, including high energy density, elevated operating voltage, eco-friendliness, and absence of memory effect [1]. Therefore, more attention and research interest are focused on lithium-ion batteries [2]. However, Nickel–cadmium batteries have also been widely used in direct-current power supply, distribution substation, and auxiliary power supply of rail transit vehicles for the advantages of low cost, high safety, wide temperature range, high reliability, and high mechanical strength [3,4]. Especially in rail transit, vehicle safety is always the first priority; however, there is still a lack of a Battery Management System (BMS) due to the inability to accurately estimate the state-of-charge (SOC) of the battery, because SOC estimation is the basis of BMS system development. Accurate SOC estimation can effectively prevent battery overcharging and over discharging,

improve the reliability and safety, and extend battery life [5–7]. With an increasingly urgent demand for intelligent and automated rail transit, it is necessary to carry out SOC estimation for rail transit vehicle nickel–cadmium batteries.

The existing SOC estimation methods can be divided into two categories: electrical testing and intelligent algorithm. The former includes the discharging experiment method, ampere-hour integration method, open-circuit voltage (OCV) method, internal resistance method, etc. [8,9]. The latter includes fuzzy logic, neural networks [10], and the Kalman filter method [11]. Among them, the discharging experiment method takes a long time and is an offline estimation. The main disadvantage of ampere-hour integration method is that it relies too much on an accurate SOC initial value, and the error will gradually increase in the integration process [8]. The open-circuit voltage method assumes that there is a specific functional mapping relationship between the OCV and the SOC of the battery. However, the OCV measurement of the battery usually requires a long static time, which is not conducive to online estimation. Usually, the OCV method is chosen to combine with other estimation methods to estimate the SOC. The internal resistance method obtains the functional mapping relationship between the internal resistance and SOC by measuring the internal resistance of the battery. However, the measurement of the internal resistance of the battery itself has a large error, and the internal resistance is also affected by environmental variables, such as temperature, so the application scope of this method is relatively narrow [9]. Fuzzy logic algorithms and neural network algorithms have high accuracy in SOC estimation, but they require a large amount of computation and rely on a large number of sample data [10]. The Kalman filter (KF) has the advantages of high precision and strong anti-noise interference [11]. In summary, KF is currently one of the most effective methods for battery SOC estimation and has received the most attention and applications. However, it relies on accurate battery models.

The existing battery models can be mainly divided into three categories according to different research focuses: the electrochemical model [12], thermal model (including electrothermal coupling model) [13], and performance model [14]. The electrochemical model is a battery model based on the electrochemical theory of ion diffusion and polarization effect, and the partial differential equation was used to describe the changes of electrode surface concentration and electrode overpotential inside the battery. However, it is difficult to obtain certain parameters, such as solid phase concentration and solid phase potential. Moreover, the solution of partial differential equations, which are mostly used in the design and development of high-performance batteries, is complex. Based on the conservation of energy, the thermal model is a mathematical model established based on the three thermal processes of heat generation, heat conduction, and heat loss. However, it is difficult to obtain the parameters of reversible heat and irreversible heat in the thermal model, so it is rarely used in SOC estimation, and is instead often used in the design of battery thermal management system and the study of single-battery heat production. The performance model is widely used in the study of external characteristics of batteries. The two mainstream performance models are the black box model and the equivalent circuit model [15]. Black-box models, including neural networks, fuzzy logic, and support vector machines, rely on a large number of sample data and have a large amount of computation. BMS system chips are difficult to meet their computational requirements. The equivalent circuit model simulates the external characteristics of a battery based on the experimental data of battery charging and discharging, using electrical components such as capacitors, resistors, and constant voltage sources. It has the advantages of a simple model, the easy identification of parameters, low computational complexity, and high accuracy, and is widely used in SOC estimation. It should be emphasized that the existing battery equivalent circuit model is mainly for lithium batteries, while the main reactions and side reactions and working characteristics of nickel–cadmium batteries are significantly different from those of lithium batteries, so there is a lack of mature models for reference at present.

Therefore, by analyzing the basic characteristics of nickel–cadmium batteries, an equivalent circuit model of nickel–cadmium battery was established, the model parameters were

identified, and the accuracy of the model was verified by experimental data and simulation. Then, based on the constructed equivalent circuit model, a SOC estimation method of Ni-Cd batteries based on adaptive unscented Kalman filter (AUKF) is proposed, and the results are compared with unscented Kalman filter (UKF) under different operating conditions.

2. Equivalent Circuit Model of Nickel–Cadmium Battery

2.1. Selection of Equivalent Circuit Model

The existing battery equivalent circuit models mainly include the Rint model, Thevenin model, DP model, PNGV model, circuit model with hysteresis characteristics, GNL model, etc. [11,16]. Based on the analysis of the existing models, it was found that when establishing the model, it is necessary to analyze whether the battery has typical hysteresis characteristics, determine the main polarization effects in the battery, and consider the complexity of model parameter identification. Based on this, the open-circuit voltage (OCV) and electrochemical impedance spectroscopy (EIS) were tested for nickel–cadmium batteries [17] so as to select the equivalent circuit model.

2.1.1. Open-Circuit Voltage Characteristic Analysis

There is a functional mapping relationship between the open-circuit voltage and the state-of-charge of a battery [18]. The common ways to obtain the OCV data are the intermittent charging and discharging experimental method and the micro-current method [19,20]. The OCV-SOC curves obtained by the two methods are different, which directly affect the subsequent model establishment and parameter identification of nickel–cadmium batteries. Therefore, in this sub-section, the reliability and applicability of these two kinds of experiments to obtain open-circuit voltage data of nickel–cadmium batteries are compared and analyzed.

The LPH160 A single nickel–cadmium battery used by China Railway Highspeed Electric Multiple Unit was selected as the experimental sample. The battery was charged and discharged by CT-4002 battery tester, and the data were recorded by Neware BTS8.0 upper computer software.

Before conducting intermittent charging and discharging experiments, it is necessary to analyze the intermittent point of the incubation time. The battery was charged at a constant current of 0.2 C to the cutoff voltage of 1.7 V and then stood, and the battery was discharged at a constant current of 0.2 C to the cutoff voltage of 1.0 V and stood, so as to obtain the variation of the static voltage in the full discharging state, as shown in Figure 1. From Figure 1, it can be seen that when the battery is put to rest after the termination of charging or discharging, it will show obvious voltage rebound characteristics, which shows that the voltage will gradually rise after the termination of discharge and the voltage will gradually decrease after the termination of charge. Therefore, the open-circuit voltage measured is relatively accurate after the voltage is stabilized. Table 1 shows the variation of the static voltage data with full release state. Combined with Figure 1, it can be seen that the average voltage change rate is 0.31 mV/min within 30 min to 60 min, and the static voltage reaches relatively stable after 30 min. Therefore, in the intermittent charging and discharging experiments, the standing time of the intermittent point is set to 30 min, which ensures the accuracy of the open-circuit voltage measurement and the continuity of the experiments.

After determining the standing time of the intermittent point, the experimental steps were set as follows: charge the fully discharged battery with constant current of 0.2 C (32 A) to 1.7 V, and then turn to constant voltage charging until the current decreases to 0.02 C (3.2 A). The battery was considered to be in a fully charged state at this time, and the total capacity of the battery was recorded. Discharge the battery at a 0.2 C constant current with a discharging capacity of 10% of the total capacity, and after standing for 30 min, record the open-circuit voltage. Repeat the discharging step nine times. After the last discharging process, when the discharging voltage reaches 1 V, the battery is considered to be in a fully discharged state at this time.
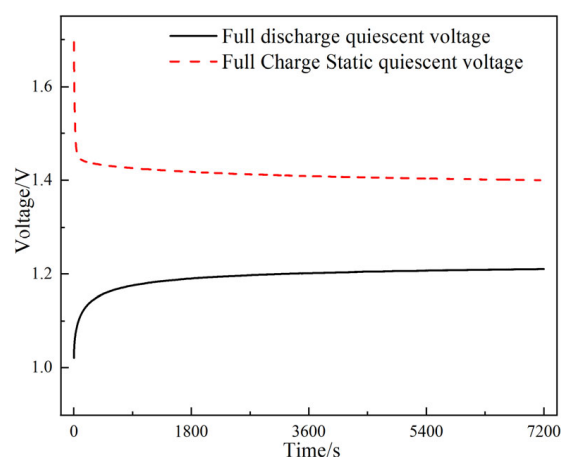
Figure 1. Static voltage variation curve at full charging/discharging process.

Table 1. Static voltages at different times in full charging/discharging state.

| Time	3 min	10 min	20 min	30 min	60 min	120 min
charging state/V	1.4394	1.4295	1.4226	1.4180	1.4087	1.4
discharging state/V	1.1297	1.1656	1.1821	1.1904	1.2013	1.2103

Similarly, charge the fully discharged battery at a constant current of 0.2 C with the charging capacity to 10% of the total capacity; Then, after standing for 30 min, record the charging open-circuit voltage. Repeat the charging steps nine times. For the last charging process, set the charging cut-off voltage to 1.7 V and cut-off current to 3.2 A. When the charging current reaches 3.2 A, the battery is considered to be in a fully charged state.

According to the above steps, the open-circuit voltage data of each SOC point are obtained, and the average value of the charging open-circuit voltage U_{coc} and the discharging open-circuit voltage U_{doc} is the equilibrium potential at this point. The difference between the equilibrium potential and the open-circuit voltage of charging and discharging is the hysteresis voltage U_h. The curves of open-circuit voltage and balanced potential are shown in Figure 2. It can be seen that at the same SOC point, the open-circuit voltage in the charging state of nickel–cadmium battery is greater than that in the discharging state, indicating that nickel–cadmium battery has typical voltage hysteresis characteristics [21]. Therefore, it is necessary to consider the hysteresis voltage when establishing its equivalent circuit model.
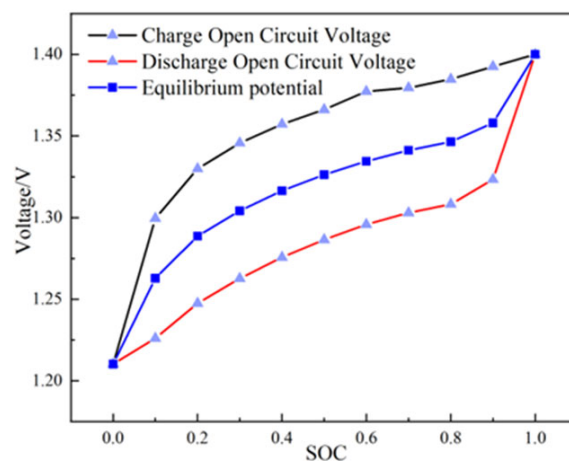
Figure 2. OCV-SOC curve of charging and discharging.

The open-circuit voltage curve obtained by the micro-current method is continuous, which is aimed to minimize the internal polarization effect and ensure the approximate symmetry of the charging and discharging curve. Then, the OCV-SOC curve is obtained by averaging the charging and discharging curve. The experimental procedure is set as follows: Discharge the fully charged battery at 0.04 C with the cut-off voltage of 1 V, and record the discharging process voltage data. Charge the fully discharged battery with constant current of 0.04 C and the cut-off voltage of 1.7 V, and record the voltage data during the charging process. The voltage–current curve of the micro-current method is shown in Figure 3. It can be seen that even when the battery is charged and discharged with a small current of 0.04 C, the voltage changes greatly in the early and late charging and discharging stages, which cannot meet the approximate symmetry of the charging and discharging curve. This is far from the voltage data obtained by intermittent charging and discharging experiments for a long time, so it is not suitable to obtain the OCV-SOC curve of nickel–cadmium battery by micro-current method. Therefore, in the identification of open-circuit voltage data, the intermittent charging and discharging experiment method is selected to obtain the open-circuit voltage of specific SOC points of the battery, and the corresponding open-circuit voltage of each SOC point is obtained by function fitting.
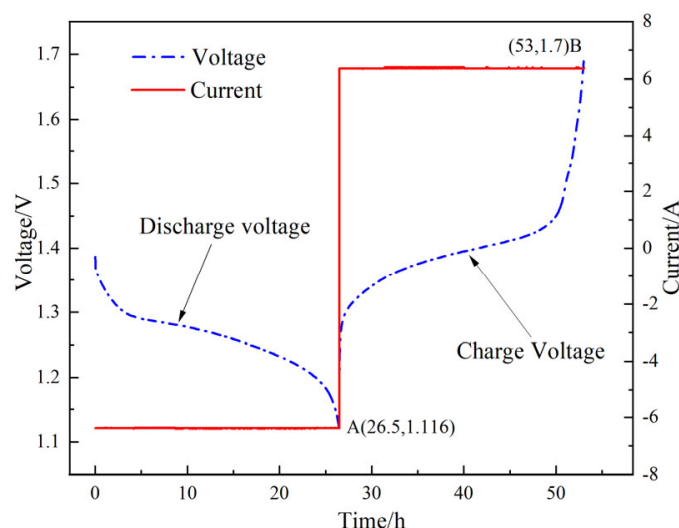
Figure 3. Voltage and current curve of the micro-current method.

2.1.2. Analysis of Polarization Effect

The EIS test can determine the actual impedance of the battery at each SOC point through the impedance curve, and then analyze the actual electrochemical process inside the battery. Through the EIS test, the order of the resistance–capacitance (RC) network of the equivalent circuit model can be determined. The nickel–cadmium battery used in the experiment was charged and discharged to different SOC points, and the alternating excitation signals with different frequencies were applied at different SOC points to obtain the corresponding frequency response signals. As shown in Figure 4, it is the EIS spectrum of nickel–cadmium battery at different SOC points, where the horizontal axis is the real part of impedance, and the vertical axis is the virtual part of impedance. It can be seen that the impedance spectrum mainly includes three parts: The first part, shown by the rectangular dotted line, that is, the area where the impedance curve intersects the horizontal axis, is the ohmic impedance R_0. Combined with Figure 4, it can be seen that the ohmic impedance of the nickel–cadmium battery is about 0.5 milliohm. The second part is selected by the oval dotted line box and represents the charge transfer impedance. If we zoom in locally on the part as shown in Figure 4, we can see more clearly that nickel–cadmium batteries have an arc section under each SOC. And the radius of the arc is not the same, that is, the charge transfer impedance under each SOC is different. The electrochemical polarization

impedance is composed of the charge transfer impedance and the interface capacitance of the electrode solution, which indicates that the electrochemical polarization effect inside the nickel–cadmium battery cannot be ignored. The third part, the following straight lines of each EIS curve in Figure 4, is called diffusion impedance, also known as concentration polarization impedance, which indicates that the concentration polarization effect cannot be ignored. Therefore, ohmic polarization, electrochemical polarization, and concentration polarization should be considered simultaneously when establishing the equivalent circuit model of nickel–cadmium battery.
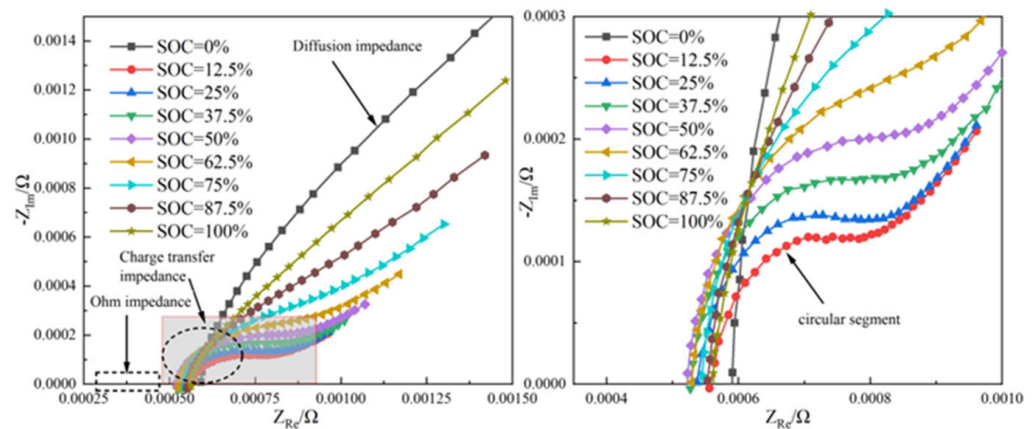

Figure 4. EIS curve under different SOCs (**left**) and local amplification (**right**).

2.1.3. Establishment of Equivalent Circuit Model

Based on the above characteristic analysis for nickel–cadmium batteries, the voltage hysteretic characteristics should be taken into account when establishing its equivalent circuit model, which should include ohmic polarization, electrochemical polarization, and concentration polarization, while also taking into account the difficulty of parameter identification of the equivalent circuit model. The equivalent circuit of nickel–cadmium batteries, as shown in Figure 5, was established.
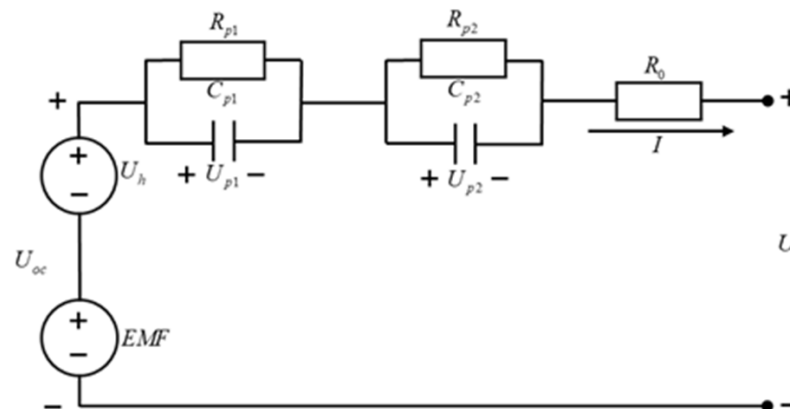

Figure 5. Equivalent circuit of nickel–cadmium battery.

In Figure 5, R_0 is ohmic impedance; R_{p1} and C_{p1} are electrochemical polarization impedance; R_{p2} and C_{p2} are concentrated polarization impedance; EMF refers to the actual balance potential of the same SOC point when charging and discharging, which is a function of SOC; and U_h is the hysteresis voltage, which describes the voltage hysteresis

characteristics during charging and discharging, and is also a function of SOC, which is the actual open-circuit voltage of the battery. The three parameters satisfy Equation (1).

$$\begin{cases} U_{oc\_cha} = \text{EMF} + U_h \\ U_{oc\_dch} = \text{EMF} - U_h \end{cases} \tag{1}$$

where U_{oc_cha} stands for charging balance potential, and U_{oc_dch} stands for discharging balance potential. The model state equation is shown in Equation (2).

$$\begin{cases} \dot{U}_{p1} = \frac{I}{C_{p1}} - \frac{U_{p1}}{R_{p1}C_{p1}} \\ U = U_{oc} - U_{p1} - U_{p2} - IR_0 \\ \dot{U}_{p2} = \frac{I}{C_{p2}} - \frac{U_{p2}}{R_{p2}C_{p2}} \end{cases} \tag{2}$$

2.2. Model Parameter Identification

There are five parameters to be identified in the above model: open circuit voltage, electrochemical polarization impedance R_{p1} and C_{p1}, concentration polarization impedance R_{p2} and C_{p2}. Compared to the intermittent charging and discharging experiment, the HPPC test [22] only has one more impulse response at each SOC point. Therefore, it is possible to stand for half an hour at the end of each pulse in the HPPC test, and the terminal voltage of the battery at the end of the standing is used as the corresponding open-circuit voltage under this SOC.

2.2.1. HPPC Test

For HPPC test protocols, refer to the FreedomCAR Battery Test Manual. Due to the typical charging and discharging voltage platform of nickel–cadmium batteries, the terminal voltage changes greatly in the early and late stages of charging and discharging, so it is necessary to reduce the charging and discharging capacity interval in the early and late stages to obtain more open-circuit voltage data points and improve the accuracy of the OCV-SOC curve. The SOC is set to a charging and discharging capacity interval of 10% in the range of 0.2 to 0.8, and the rest of the SOC is set to charging and discharging capacity interval of 5%. The battery HPPC test curve is shown in Figure 6.
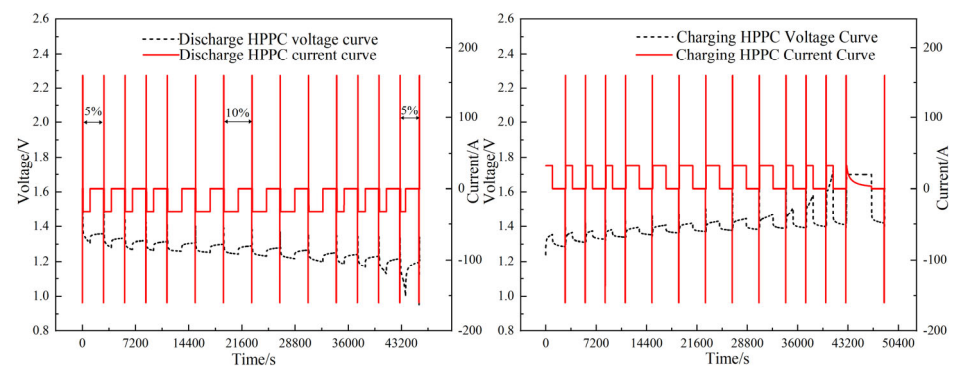

Figure 6. HPPC discharging test and charging test.

From Figure 6, at the end of discharging, the terminal voltage changes significantly, and the terminal voltage will quickly decrease to the cut-off voltage.

2.2.2. Open-Circuit Voltage Identification

According to the open-circuit voltage data of each SOC point obtained by the HPPC test and Equation (1), the equilibrium potential and hysteresis voltage can be obtained. Since the accuracy of the OCV-SOC curve directly affects the accuracy of the model, eighth-

order polynomials are selected for function-fitting to ensure the accuracy of fitting. The fitting results are shown in Figure 7.
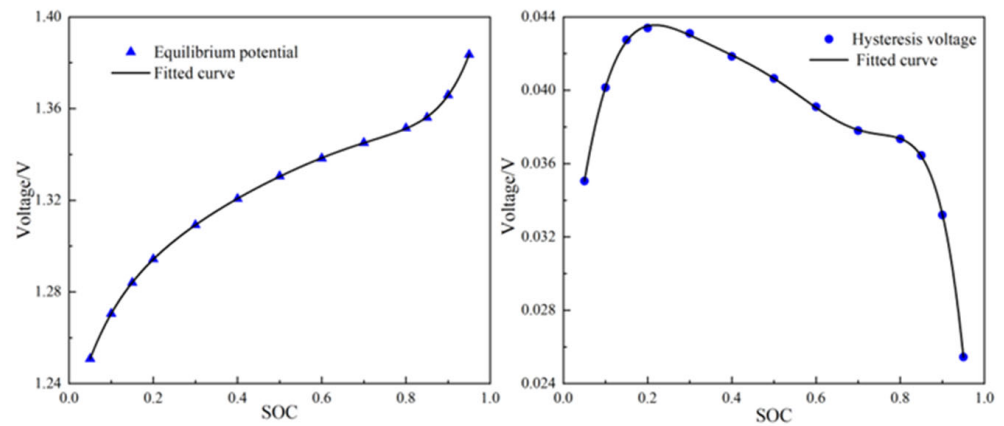

Figure 7. The fitting curves of equilibrium potential and hysteretic voltage.

From Figure 7, the eighth-order polynomial can fit the data at each SOC point well, and the determination coefficients R^2 of the equilibrium potential and hysteresis voltage curves are 0.9999 and 0.99987, respectively. The fitting function is shown in Equation (3):

$$
\begin{cases}
\text{EMF(SOC)} = -0.68175\text{SOC}^8 + 8.82823\text{SOC}^7 - 24.43179\text{SOC}^6 + 31.87221\text{SOC}^5 \\
\quad -23.97881\text{SOC}^4 + 11.24774\text{SOC}^3 - 3.40685\text{SOC}^2 + 0.74692\text{SOC} + 1.22076 \\
U_h(\text{SOC}) = 2.62496\text{SOC}^8 - 12.77132\text{SOC}^7 + 22.37586\text{SOC}^6 - 18.04921\text{SOC}^5 \\
\quad +6.14667\text{SOC}^4 + 0.26467\text{SOC}^3 - 0.82125\text{SOC}^2 + 0.21246\text{SOC} + 0.02641
\end{cases}
\tag{3}
$$

2.2.3. Identification of Resistance and Capacitance

In the HPPC test, a pulse current is applied at each SOC point, and the corresponding impulse response voltage of the battery is obtained. The impulse voltage response when SOC = 0.5 is shown in Figure 8, and the resistance capacitance parameters are identified according to the impulse response.
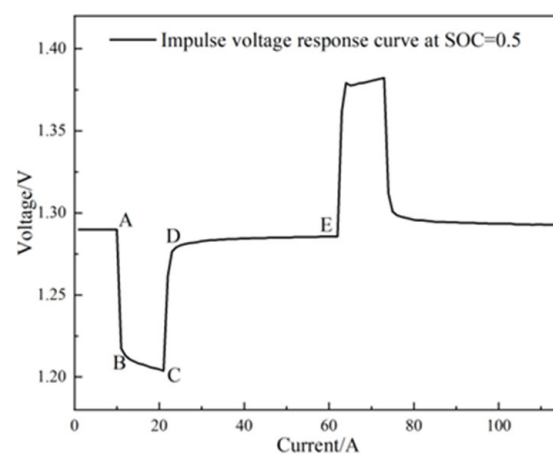
Figure 8. Pulse voltage response at SOC = 0.5.

From Figure 8, before section AB, the battery was in a static state, and the capacitor voltage was 0. At the moment of pulse-current loading, the sudden voltage was mainly caused by the ohmic internal resistance, so section AB was used to calculate the ohmic internal resistance R_0.

$$
R_0 = \frac{U_A - U_B}{I}
\tag{4}
$$

Before the BC segment, the battery is in a static state, and the initial state of the capacitor can be considered to be zero, so the capacitor in the BC segment is in a zero-state response. The voltage-response formula of the capacitor in the BC segment is shown in Equation (5).

$$U_p(\text{t}) = IR_p(1 - e^{-\frac{t-t_A}{\tau}})$$ (5)

In the DE segment, the battery is in the static stage after pulse-current unloading, the current is zero, and the capacitor is zero-input response. The capacitor voltage response formula in the DE segment is shown in Equation (6).

$$U_p(t) = U_p(t_c)e^{-\frac{t-t_C}{\tau}}$$ (6)

Therefore, according to Kirchhoff's Voltage Law, the function expression of the terminal voltage of the DE segment is as follows:

$$U(t) = U_{oc} - U_{p1}(t_c)e^{-\frac{t-t_C}{\tau_1}} - U_{p2}(t_c)e^{-\frac{t-t_C}{\tau_2}}$$ (7)

Equation (7) is an exponential function of terminal voltage with respect to time. MATLAB fitting toolbox was used to perform exponential function-fitting on the measured DE-segment voltage data, and the fitting formula is shown in Equation (8).

$$y(x) = A - Be^{-bx} - Ce^{-cx}$$ (8)

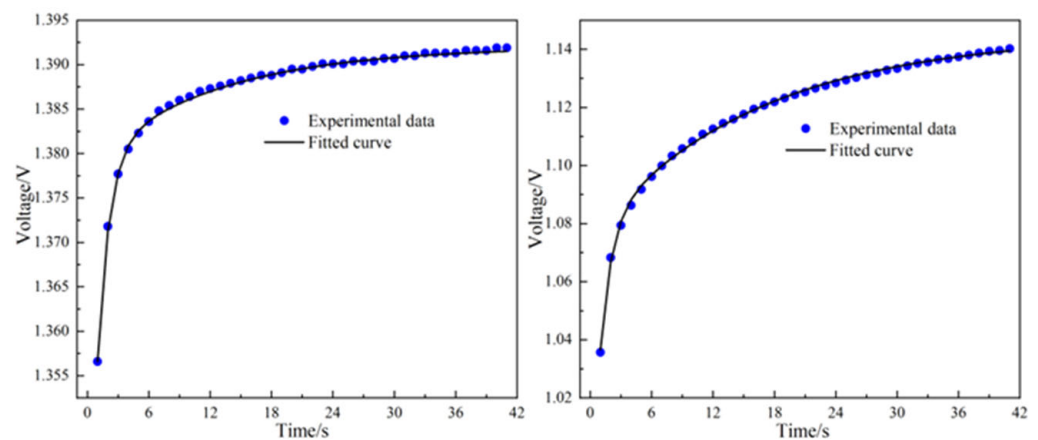The voltage-fitting curve at the end of DE segment is shown in Figure 9.

Figure 9. DE segment terminal voltages at SOC = 1 and SOC = 0.

From Figure 9, the selected fitting formula can fit the terminal voltage data of the DE segment well, and the fixed coefficients R^2 of the two curves are 0.9999 and 0.9999, respectively, showing a good fitting effect.

The specific values of A, B, C, b, and c in Equation (8) can be obtained according to the fitted exponential function. The polarization resistance and corresponding time constant can be obtained by Equations (6)–(8), as shown in Equation (9).

$$\begin{cases} R_{p1} = \dfrac{B}{I\left(1-e^{-\frac{t_C-t_A}{\tau_1}}\right)}, \tau_1 = \dfrac{1}{b} \\ R_{p2} = \dfrac{C}{I\left(1-e^{-\frac{t_C-t_A}{\tau_2}}\right)}, \tau_2 = \dfrac{1}{c} \end{cases}$$ (9)

For RC networks, the time constant and resistance capacitance satisfy Equation (10).

$$\begin{cases} \tau_1 = R_{p1}C_{p1} \\ \tau_2 = R_{p2}C_{p2} \end{cases} \tag{10}$$

Parameter identification results can be obtained by using Equations (9) and (10) simultaneously and substituting the exponential function coefficient and current data obtained by fitting, as shown in Table 2.

Table 2. Identification results of resistance and capacitance parameters at each SOC point.

| SOC	$R_{p1}/m\Omega$	$R_{p2}/m\Omega$	C_{p1}/F	C_{p2}/F	$R_0/m\Omega$	R^2
0	0.6862	0.9412	1579.2	17,270	0.575625	0.9990
0.05	0.5871	0.4424	1406.5	32,277	0.5425	0.9987
0.1	0.4799	0.2187	1553.9	57,450	0.505625	0.9986
0.15	0.5509	0.1372	1196.6	82,769	0.498125	0.9987
0.2	0.5225	0.1126	1268.3	118,287	0.484375	0.9990
0.3	0.5353	0.0873	1156.7	132,594	0.464875	0.9975
0.4	0.5516	0.0719	1100.1	138,528	0.4575	0.9975
0.5	0.6581	0.0734	837.7	126,735	0.453125	0.9986
0.6	0.5963	0.0707	998.2	129,289	0.45125	0.9984
0.7	0.5729	0.0735	1086.9	130,195	0.45125	0.9986
0.8	0.5421	0.0841	1267.8	126,362	0.453125	0.9972
0.85	0.5269	0.0987	1378.3	129,231	0.4575	0.9983
0.9	0.5754	0.1015	1206.9	90,553	0.474375	0.9985
0.95	0.5269	0.1239	1525.6	88,407	0.49375	0.9987
1	0.3519	0.1484	3236.4	85,061	0.51625	0.9990

2.3. Model Simulation and Verification

According to the parameter identification results, the equivalent circuit simulation model of the nickel–cadmium battery was established in Simulink, as shown in Figure 10. The current value and measured voltage value are, respectively introduced into two signal generators, and the SOC is preliminarily calculated using the amp-hour integration method. According to Equation (3), the fitting function is obtained to calculate the corresponding open-circuit voltage under different SOC points. Meanwhile, the parameter lookup module is used to calculate the corresponding ohm internal resistance, polarization resistance, polarization capacitance, and other parameter values under each SOC, and then the partial voltage is calculated according to the parameter values. Finally, the terminal voltage is calculated according to Equation (2). Based on HPPC test, the measured value of terminal voltage was compared with the simulated value of terminal voltage, and the accuracy of the model was analyzed from the pulse response stage and the constant current discharging stage, respectively.
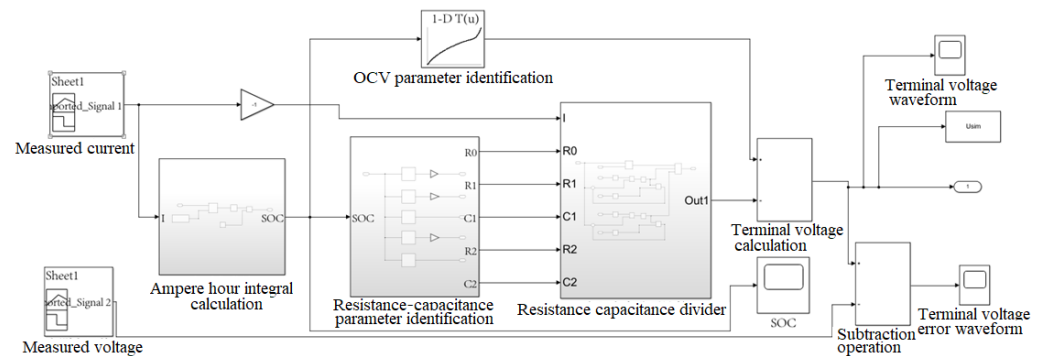
Figure 10. Equivalent circuit simulation model.

The measured and simulated terminal voltage values under HPPC conditions are shown in Figure 11a. Then, the absolute error curve shown in Figure 11b and the relative error curve shown in Figure 11c can be obtained. It can be seen from Figure 11a that the simulation value can dynamically change with the measured value under the whole working condition. It can be seen from Figure 11b that the error increases significantly at the end of discharging because the internal parameters of the battery change greatly and the voltage changes are noticeable at the end of discharging. It can be seen in Figure 11c that the relative error remains within 1% most of the time, and the maximum value is 5% at the end of the discharging period.
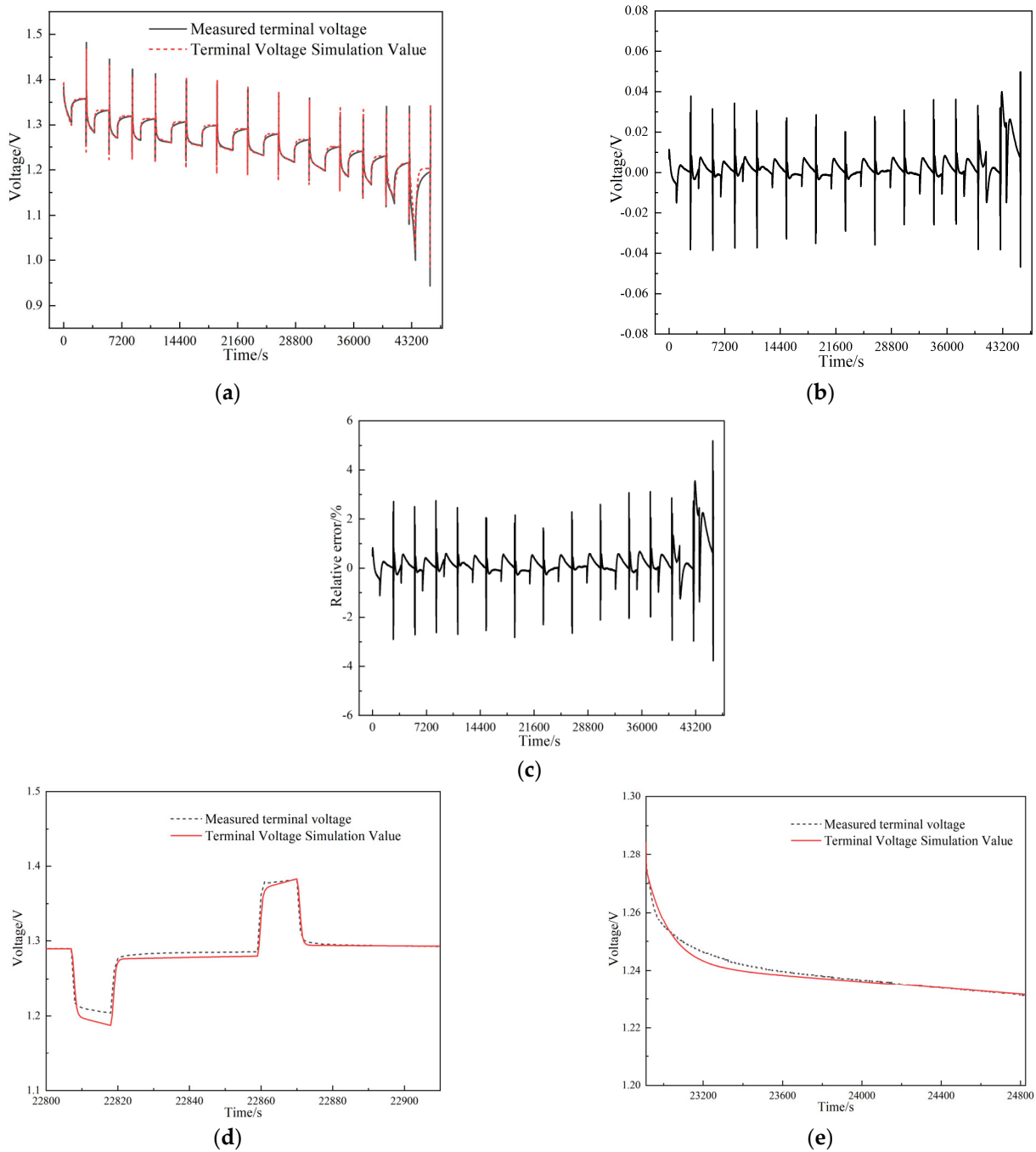
Figure 11. (**a**) Terminal voltage; (**b**) absolute terminal voltage error; (**c**) relative error; (**d**) terminal voltage in pulse phase; (**e**) terminal voltage in constant discharge phase.

Figure 11d,e presents the terminal voltage variation curves of the pulse stage and the constant-current discharge stage at SOC = 0.5. It can be seen that the terminal voltage error in the pulse stage is slightly larger than that in the constant-current discharging stage. Because the internal pulse response mechanism of the battery is complex, the measured value error will increase slightly.

Three parameters of root mean square error (RMSE), maximum absolute error (MaxAE), and mean absolute error (MAE) as Equation (11) are used to quantitatively evaluate the modeling effectiveness. The calculation results are listed in Table 3.

$$
\begin{cases}
\text{RMSE} = \sqrt{\dfrac{1}{L}\sum\limits_{k=1}^{L}\left(U_k - U_k'\right)^2} \\
\text{MaxAE} = \max\left(\left|U_k - U_k'\right|\right) \\
\text{MAE} = \dfrac{\sum\limits_{k=1}^{L}\left|U_k - U_k'\right|}{L}
\end{cases}
\tag{11}
$$

Table 3. Error results at different stages under HPPC working conditions.

	HPPC Working Condition	Pulse Phase at SOC = 0.5	Constant Current Phase at SOC = 0.5
MAE/mV	4.047	5.995	1.067
RMSE/mV	7.401	8.721	1.504
MaxAE/mV	49.790	29.040	4.040

In Equation (11), L is the sample number, and U_k and U_k' represent the measured and simulated values of the terminal voltage, respectively.

From Table 3, MAE and RMSE are 4.047 mV and 7.4012 mV, respectively, with high accuracy. MaxAE is 49.79 mV, which appears in the pulse discharge stage at SOC = 0. The error is large at this time because the discharging at the cut-off voltage causes over discharging. At this time, the terminal voltage changes sharply. Meanwhile, the error value of the constant current stage is smaller than that of the pulse stage, with an MAE and RMSE value of 1.067 mV and 1.50471 mV, respectively, indicating that the accuracy of the established simulation model meets the requirements and can better simulate the working characteristics of nickel–cadmium battery.

3. AUKF Estimation Algorithm

In Section 2, the equivalent circuit model of the nickel–cadmium battery was established. Based on the model and KF algorithm, the SOC of the nickel–cadmium battery can be estimated. The standard KF algorithm is a pure time-domain filter, which has the advantages of a simple structure and good robustness. However, it is only suitable for the modeling analysis of linear systems. The nickel–cadmium battery has polarization effect and diffusion effect in its internal and nonlinear external performance, so it is necessary to use the improved Kalman filter algorithm. At present, the commonly improved forms are the extended Kalman filter (EKF) and unscented Kalman filter (UKF) [23]. When the EKF algorithm performs Taylor expansion on the nonlinear part, it will produce a Taylor truncation error and may make the filter difficult to converge and increase the error. Moreover, the EKF algorithm needs to calculate the Jacobian matrix once in each iteration process, which increases the amount of calculations. The UKF algorithm [24–26] can also be used for the state estimation of nonlinear systems. Its core method is unscented transformation (UT) [27,28], in which sampling points are used to approximate the distribution of nonlinear state variables, without the linearization of nonlinear functions and Jacobian matrix solution. Compared to the EKF algorithm, the UKF algorithm has a simpler principle, higher accuracy, less computation, and wider application.

3.1. UKF Algorithm

The discrete state space model of linear system is generally composed of state equation and observation equation, and the general expression is shown in Equation (12).

$$\begin{cases} x_{k+1} = Ax_k + Bu_k + w_k \\ y_k = Cx_k + Du_k + v_k \end{cases} \tag{12}$$

where x_k is the state quantity at time k; x_{k+1} is the state quantity at the next time; u_k is the system input quantity; y_k is the system observation value at time k; and A, B, C, and D are the state transition matrix, input matrix, output matrix, and feedforward matrix of the system, respectively; w_k and v_k refer to process noise and observation noise, respectively, which are generally set as Gaussian white noise, as shown in Equation (3).

$$\begin{cases} w_k \sim N(0, Q_k) \\ v_k \sim N(0, R_k) \end{cases} \tag{13}$$

where $Q_k(R_k)$ is the covariance matrix of process noise (observation noise).

The UT in the UKF algorithm [27,28] is used to sample near the state points of nonlinear functions with reference to certain sampling strategies. The sampling points are collectively referred to as the sigma point set. The sigma point set and the state variables of the original state distribution have the same mean and variance. The sigma point set is substituted into the original nonlinear function relationship for nonlinear transfer, and the nonlinear function value point set is calculated. The mean and covariance of the transformed point set are further calculated. The UKF algorithm can approximate the mean and covariance to the third-order Taylor series. For the n-dimensional state variable, x, $\overline{x}$, and P are used to represent the mean and variance of the state variable, respectively. Firstly, $2n + 1$ sampling points are obtained by using the symmetrical sampling strategy, and then the corresponding weights of each sampling point are calculated. Finally, the mean and covariance of the output variable are obtained. The specific steps are as follows:

(1) Calculate $2n + 1$ sampling points according to Equation (14).

$$\begin{cases} x_0 = \overline{x} \\ x_i = \overline{x} + (\sqrt{(n+\lambda)P_x})_i, i = 1, 2, 3, \cdots, n \\ x_i = \overline{x} - (\sqrt{(n+\lambda)P_x})_i, i = n+1, n+2, \cdots, 2n \end{cases} \tag{14}$$

where n refers to the dimension of the state variable, x_i refers to sigma point i, $\left(\sqrt{(n+\lambda)P_x}\right)_i$ refers to the number i column of the root mean square of the $(n+\lambda)P_x$ matrix, λ refers to the scale adjustment factor, and the distance between the sampling point and the mean x can be adjusted by changing λ so as to adjust the accuracy of the algorithm.

(2) Calculate the weight corresponding to each sampling point.

$$\begin{cases} w_m^0 = \lambda/(n+\lambda) \\ w_c^0 = [\lambda/(n+\lambda)] + (1+\beta-\alpha^2) \\ w_c^i = 1/[2(n+\lambda)], i = 1, 2, 3 \cdots, 2n \\ w_m^i = 1/[2(n+\lambda)], i = 1, 2, 3 \cdots, 2n \\ \lambda = \alpha^2(n+k) - n \end{cases} \tag{15}$$

In Equation (15), w_m is the mean weight; w_c represents covariance weight; α is the dispersion degree factor, which is used to describe the dispersion of sampling points around the mean $\overline{x}$ and meets the relationship $10^{-6} \leq \alpha < 1$; k is the auxiliary scale factor, usually taken as 0 or $3 - n$; and β is the prior distribution factor, which is used to suppress the error caused by higher-order terms. For Gaussian distribution, the best result can be obtained when $\beta = 2$ is taken.

(3) Calculate the mean $\bar{y}$ and covariance P_y of the output variable.

$$
\begin{cases}
\bar{y} = \sum\limits_{i=0}^{2n} w_m{}^i y_i \\
P_y = \sum\limits_{i=0}^{2n} w_c{}^i (y_i - \bar{y})(y_i - \bar{y})^T
\end{cases}
\tag{16}
$$

Based on UT, the detailed steps of UKF algorithm can be obtained as follows:
(1) Initialize the calculation of state variable x_0 and covariance P_0.

$$
\hat{x}_0 = E[x_0]
\tag{17}
$$

$$
P_0 = E[\tilde{x}_0 \tilde{x}_0{}^T]
\tag{18}
$$

(2) Combined with UT, calculate the sigma point sets using the symmetrical sampling strategy.

$$
\begin{cases}
x_{k-1}^0 = \hat{x}_{k-1} \\
x_{k-1}^i = \hat{x}_{k-1} + (\sqrt{(n+\lambda)P_x})_i, i = 1, 2, 3, \cdots, n \\
x_{k-1}^i = \hat{x}_{k-1} - (\sqrt{(n+\lambda)P_x})_i, i = n+1, n+2, \cdots, 2n
\end{cases}
\tag{19}
$$

(3) Substitute the sigma point sets into the state equation to complete the backward propagation of the sigma point sets.

$$
x_{k|k-1}^i = f(x_{k-1}^i, u_{k-1})
\tag{20}
$$

(4) According to the weight corresponding to the sigma point sets, complete the prediction of the state quantity and the calculation of the covariance matrix.

$$
\begin{cases}
\hat{x}_{k|k-1} = \sum\limits_{i=0}^{2n} w_m^i x_{k|k-1}^i + q_k \\
P_{k|k-1} = \sum\limits_{i=0}^{2n} w_c^i (x_{k|k-1}^i - \hat{x}_{k|k-1})(x_{k|k-1}^i - \hat{x}_{k|k-1})^T + Q_k
\end{cases}
\tag{21}
$$

In Equation (21), q_k is the average value of process noise.
(5) Substitute the sigma point sets into the observation equation to calculate the system observation value.

$$
y_{k|k-1}^i = h(x_{k-1}^i, u_{k-1})
\tag{22}
$$

(6) According to the weight corresponding to sigma point set, complete the prediction of observation and the calculation of covariance and cross covariance matrix.

$$
\begin{cases}
\hat{y}_{k|k-1} = \sum\limits_{i=0}^{2n} w_m^i y_{k|k-1}^i + r_k \\
P_{x_k y_k} = \sum\limits_{i=0}^{2n} w_c^i (x_{k|k-1}^i - \hat{x}_{k|k-1})(y_{k|k-1}^i - \hat{y}_{k|k-1})^T \\
P_{y_k y_k} = \sum\limits_{i=0}^{2n} w_c^i (y_{k|k-1}^i - \hat{y}_{k|k-1})(y_{k|k-1}^i - \hat{y}_{k|k-1})^T + R_k
\end{cases}
\tag{23}
$$

In Equation (23), r_k is the average value of observation noise.
(7) Obtainthe Kalman gain matrix from the covariance matrix.

$$
K_k = P_{x_k y_k} P_{y_k y_k}^{-1}
\tag{24}
$$

(8) Update the system state matrix and its covariance matrix

$$
\begin{cases}
\hat{x}_k = \hat{x}_{k|k-1} + K_k(y_k - \hat{y}_{k|k-1}) \\
P_k = P_{k|k-1} - K_k P_{y_k y_k} K^T
\end{cases}
\tag{25}
$$

3.2. AUKF Algorithm

When using UKF algorithm to deal with battery SOC estimation, it is necessary to obtain the prior system noise and observation noise information, which is set as a constant value by the standard UKF algorithm. However, there will be a certain deviation between the set constant value and the actual noise value in each iteration process, and the error will gradually accumulate with the increase in iteration times, which will reduce the estimation accuracy of the UKF algorithm, and may even lead to filtering divergence. Therefore, in order to further improve the accuracy of SOC estimation, the Sage–Husa adaptive filtering algorithm [29–32] is selected to correct the covariance of process noise and observation noise in real time. The main steps of the standard Sage-Husa adaptive filtering algorithm for noise adaptation are as follows:

(1) Calculate the estimated average value of process noise.

$$\begin{cases} \hat{q}_k = (1 - d_k)\hat{q}_{k-1} + d_k\left(\hat{x}_k - \hat{x}_{k|k-1}\right) \\ d_k = (1 - b)/(1 - b^k) \end{cases} \tag{26}$$

In Equation (26), d_k is the forgetting coefficient, and b is the forgetting factor, which generally meets the relationship $0.95 \leq b < 1$.

(2) Calculate the covariance estimated value of process noise.

$$\begin{cases} \hat{Q}_k = (1 - d_k)\hat{Q}_{k-1} + d_k(K_k e_k e_k{}^T K_k{}^T + P_k - P_{x_k y_k} P_{x_k y_k}{}^T) \\ e_k = y_k - \hat{y}_k \end{cases} \tag{27}$$

In Equation (27), e_k represents the difference between the true value of the observation value and the estimated value of the observation value at time k, which is the observation residual, also known as the innovation sequence of the observation value.

(3) Calculate the estimated average value of the observation noise

$$\hat{r}_k = (1 - d_k)\hat{r}_{k-1} + d_k(y_k - \hat{y}_{k|k-1}) \tag{28}$$

(4) Calculate the estimated covariance value of the system observation noise

$$\hat{R}_k = (1 - d_k)\hat{R}_{k-1} + d_k(e_k e_k{}^T - P_{y_k y_k} P_{y_k y_k}{}^T) \tag{29}$$

Under some special conditions (such as large current fluctuations), it is difficult to ensure that the process noise covariance matrix $\hat{Q}_k$ and the observation noise covariance matrix $\hat{R}_k$ maintain non-negative definiteness. If $\hat{Q}_k$ and $\hat{R}_k$ are negative definite, the covariance matrix P_k of the state variable will be non-semi-positive definite, resulting in the failure of the sigma sampling point calculation in the UKF algorithm and the failure of the program [33]. Therefore, $\hat{Q}_k$ and $\hat{R}_k$ are improved as follows:

$$\begin{cases} \hat{Q}_k = \sqrt{diag(diag(\hat{Q}_k \hat{Q}_k{}^T))} \\ \hat{R}_k = \sqrt{diag(diag(\hat{R}_k \hat{R}_k{}^T))} \end{cases} \tag{30}$$

In Equation (30), *diag* means to take the main diagonal elements of the original matrix to form a diagonal matrix, and Equations (26)–(30) constitute an improved Sage–Husa adaptive filtering algorithm. When combined with the UKF algorithm, it can effectively ensure the semi-positive definiteness of the state variable covariance matrix P_k so that the UKF algorithm can continue to iterate and improve the stability and persistence of filtering.

The improved Sage–Husa adaptive filtering algorithm is used to adaptively modify the noise covariance matrix in the UKF algorithm, and q_k, Q_k, r_k, and R_k in the UKF algorithm are replaced by $\hat{q}_k$, $\hat{Q}_k$, $\hat{r}_k$, and $\hat{R}_k$, respectively, to form the AUKF algorithm. The specific flow of the AUKF algorithm is shown in Figure 12.
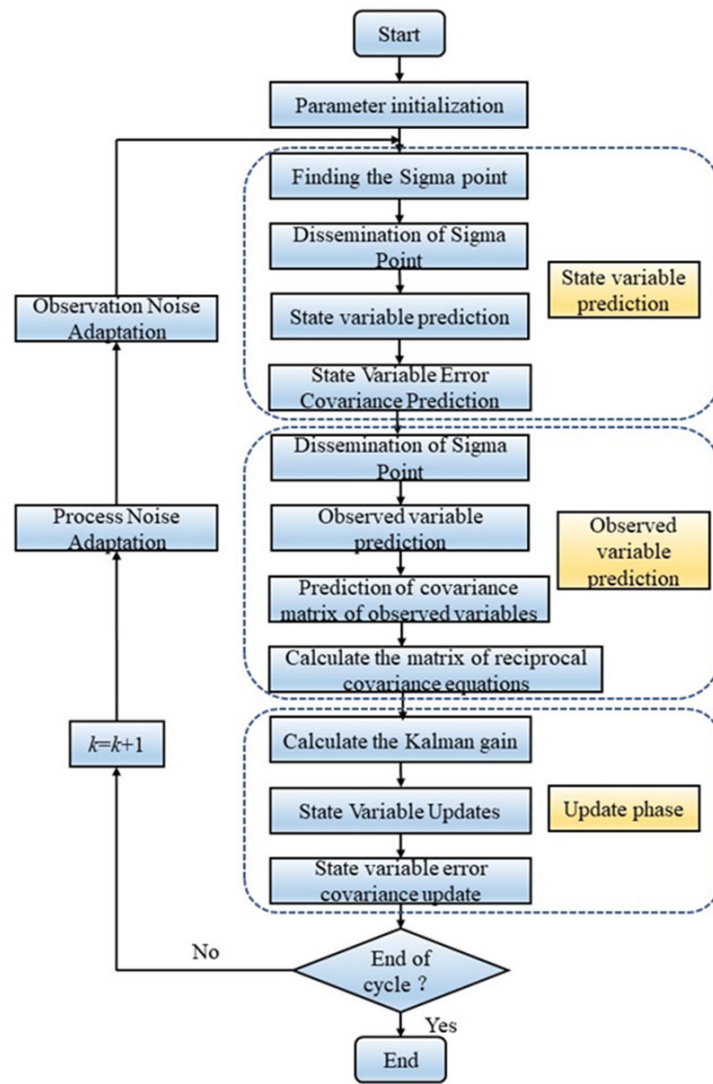
Figure 12. AUKF algorithm flow.

4. Simulation and Experimental Verification

Before using the UKF algorithm and the AUKF algorithm to estimate the SOC, the state equation and observation equation of the model need to be discretized. Based on the equivalent circuit model shown in Figure 5, the battery SOC, R_1C_1 branch voltage U_1 and R_2C_2 branch voltage U_2 are selected as the three state variables of the system, the charging and discharging current is selected as the system input value, and the battery terminal voltage is selected as the system observation value, and the battery state equation is derived, as shown in Equation (31).

$$
\begin{cases}
\dot{SOC}(t) = -\frac{1}{C_n}i(t) \\
\dot{U}_1 = -\frac{1}{R_1C_1}U_1 + \frac{1}{C_1}i(t) \\
\dot{U}_2 = -\frac{1}{R_2C_2}U_2 + \frac{1}{C_2}i(t)
\end{cases}
\tag{31}
$$

The battery observation equation is shown in Equation (32).

$$
U(t) = U_{oc}(SOC(t)) - U_1(t) - U_2(t) - i(t)R_0
\tag{32}
$$

The above equation is discretized, and the discretized equation of state is obtained, as shown in Equation (33).

$$
\begin{bmatrix} U_{1,k+1} \\ U_{2,k+1} \\ SOC_{k+1} \end{bmatrix} = \begin{bmatrix} 1 - \frac{T}{R_{1,k}C_{1,k}} & 0 & 0 \\ 0 & 1 - \frac{T}{R_{2,k}C_{2,k}} & 0 \\ 0 & 0 & 1 \end{bmatrix} \begin{bmatrix} U_{1,k} \\ U_{2,k} \\ SOC_k \end{bmatrix} + \begin{bmatrix} \frac{T}{C_{1,k}} \\ \frac{T}{C_{2,k}} \\ -\frac{T}{C_n} \end{bmatrix} I_k + w_k \tag{33}
$$

The discretized output equation is shown in Equation (34).

$$
U_k = U_{oc}(SOC_k) - U_{1,k} - U_{2,k} - I_k R_{0,k} \tag{34}
$$

The nonlinear form of the model can be further written as

$$
\begin{cases} x_{k+1} = f(x_k, u_k) + w_k = \begin{bmatrix} (1 - \frac{1}{R_{1,k}C_{1,k}})x_{1,k} + \frac{1}{C_{1,k}}u_k \\ (1 - \frac{1}{R_{2,k}C_{2,k}})x_{2,k} + \frac{1}{C_{2,k}}u_k \\ x_{3,k} - \frac{1}{C_n}u_k \end{bmatrix} + w_k \\ y_k = g(x_k, u_k) + v_k = U_{oc}(x_{3,k}) - x_{1,k} - x_{2,k} - R_{0,k}u_k + v_k \end{cases} \tag{35}
$$

The above nonlinear function is substituted into the AUKF algorithm flow, and the SOC estimation of nickel–cadmium battery is completed according to Equations (17)–(30).

4.1. SOC Estimation Verification under HPPC Test

Due to the typical voltage plateau period of nickel–cadmium battery, the voltage change during the plateau period is small, so a small voltage error may produce a large SOC error. In addition, in the actual operation of the battery, the initial value of the SOC is usually unknown, and it will spend more time to obtain the initial value of the SOC by standing for a long time, so the SOC estimation algorithm needs to be robust and can accept an initial value error within a certain range.

The initial values of covariance matrix, process noise, and observation noise are set as follows:

$$
P_0 = \begin{bmatrix} 1 & 0 & 0 \\ 0 & 1 & 0 \\ 0 & 0 & 1 \end{bmatrix}, \ Q_0 = \begin{bmatrix} 10^{-6} & 0 & 0 \\ 0 & 10^{-6} & 0 \\ 0 & 0 & 10^{-6} \end{bmatrix}, \ R_0 = 0.02 \tag{36}
$$

Two parameters, MAE and RMSE, are selected to comprehensively evaluate the performance of the two algorithms. The comparison results are shown in Table 4.

Table 4. Comparison of SOC estimation results of two algorithms under HPPC conditions.

	UKF	AUKF
MAE%	0.8958	0.4884
RMSE%	1.0372	0.4891

HPPC test steps are shown in Section 2.2.1. Before the experiment, the battery was in a fully charged and static state for a long time, and the polarization effect in the battery was not obvious. It can be considered that the initial value of RC network terminal voltage was 0, and that the initial value of the SOC was 1. When the initial value of the SOC was set to 0.7, there was an initial error of 30% with the actual initial value. The robustness and accuracy of the algorithm were tested. Figure 13 shows the estimation results of two algorithms for SOC estimation under HPPC conditions.
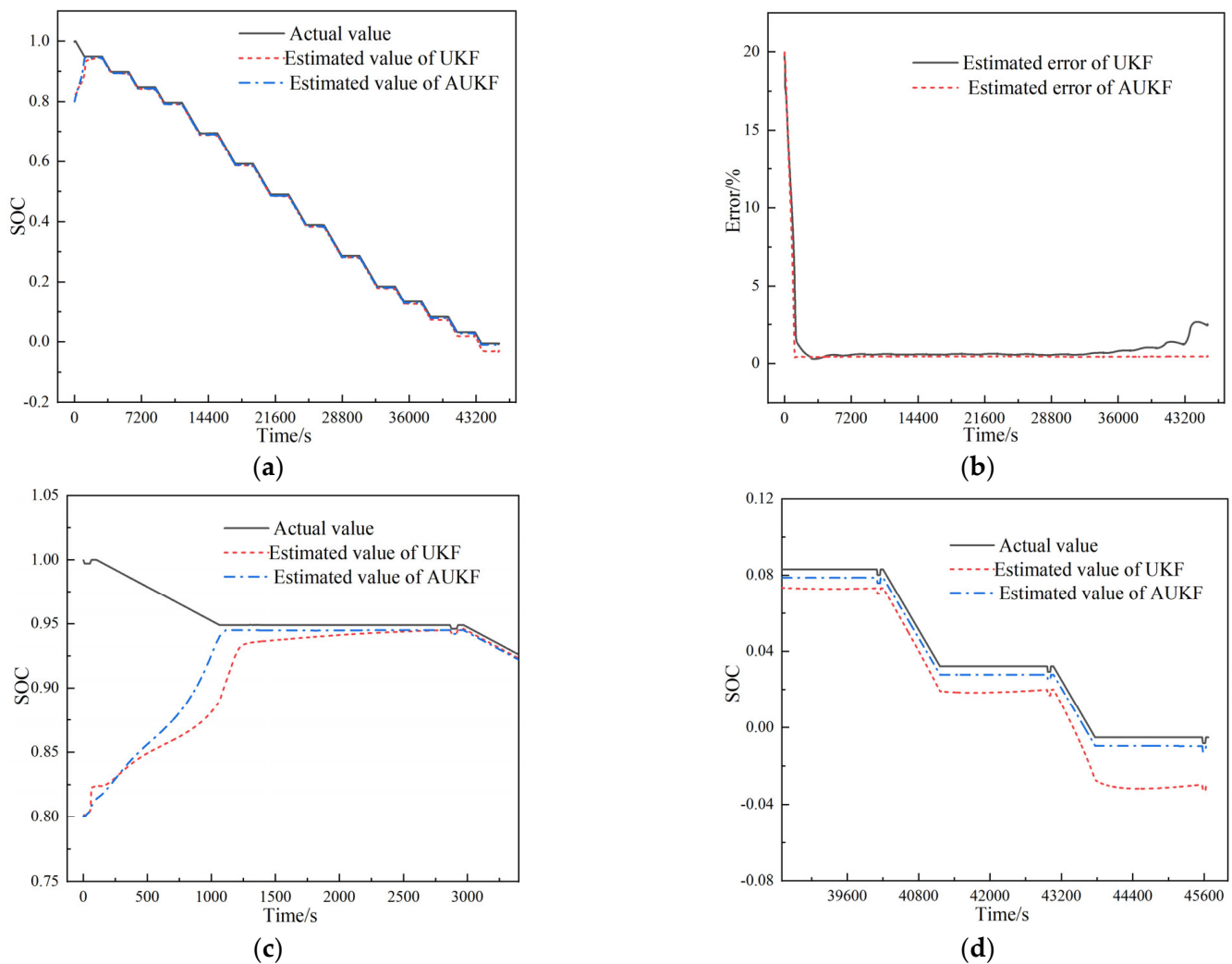
Figure 13. (**a**) SOC estimation results; (**b**)SOC estimation error; (**c**) early local amplification of SOC estimation results; (**d**) late local amplification of SOC estimation results.

Based on the analysis in Figure 13 and Table 4, the UKF algorithm and AUKF algorithm can still converge to the real value of the SOC when there is a large error in the initial value of the SOC, which has good robustness. As can be seen from Figure 13b,d, the noise error of UKF algorithm will gradually accumulate with the increase in iteration times, which shows that the error increases at the end of the working condition, and the maximum error reaches 2.93%. The AUKF algorithm updates the noise adaptively in each iteration process, and the error is smaller and more stable. Under the three initial values, MAE and RMSE are stable within 0.5%, and the accuracy is higher. Simulation results show that the AUKF algorithm has higher accuracy and robustness in estimating the SOC of the nickel–cadmium battery.
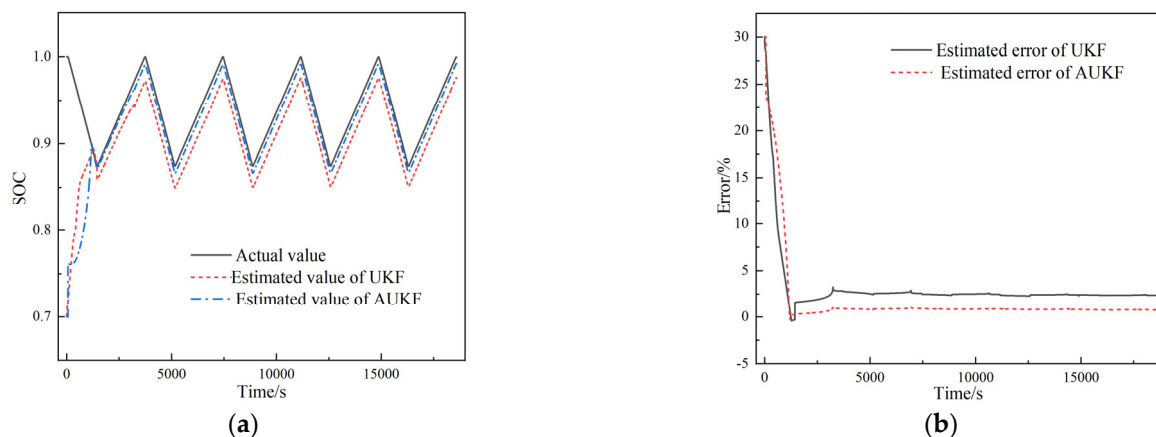
4.2. Verification of SOC Estimation under Constant Power Discharging Cycle

In the actual use of nickel–cadmium batteries, the discharging current is usually dynamic and in a state of recycling. Therefore, the constant power discharging cycle is further selected to verify the model. The discharging process is set at a constant power of 66.5 W, the charging process is set at 0.2 C constant current, the charging and discharging capacity is 20 Ah, and the cycle repeats five times. The voltage and current changes under this working condition are shown in Figure 14.
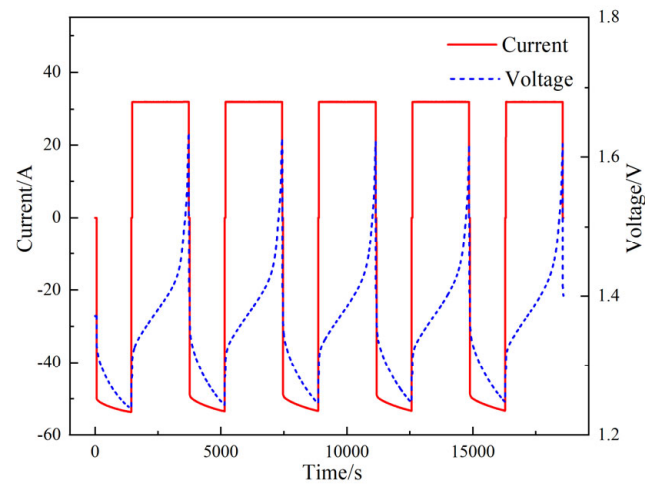
Figure 14. Voltage and current changes under charging and discharging cycle with constant power of 66.5 W.

Under this working condition, the current changes continuously during the discharging process, including both the discharging and charging processes, which tests the dynamic following ability of the algorithm. Similarly, the SOC initial value error was set to 30% to further evaluate the robustness of the algorithm under this working condition, as shown in Figure 15.

(a)

(b)

Figure 15. (**a**) SOC estimation results; (**b**) SOC estimation error.

The SOC estimation results of the two algorithms under constant power cycle are shown in Table 5.

Table 5. Comparison of SOC estimation results of two algorithms under constant power cycle.

	UKF	AUKF
MAE%	2.3922	0.7818
RMSE%	2.4146	0.7954

Based on Figure 15 and Table 5, when the battery changes from discharging to charging, the UKF estimation error becomes larger, while the AUKF can maintain a smaller error throughout the cycle. The MAE and RMSE of the AUKF algorithm in the convergence stage are always kept within 0.8%, which has good accuracy. The simulation results show that the AUKF algorithm can still maintain good dynamic following ability under cyclic conditions, and has high accuracy. Hence, the AUKF is more suitable for the SOC estimation of nickel–cadmium batteries.

5. Conclusions

In this paper, the open-circuit voltage characteristics and polarization voltage characteristics of nickel–cadmium battery were studied. It was found that the intermittent charge–discharge method used to determine the OCV-SOC curve of a nickel–cadmium battery was more applicable than the micro-current method. It showed that the nickel–cadmium battery had typical voltage hysteresis characteristics, as well as the characteristics of ohmic polarization, electrochemical polarization, and concentration polarization during the whole process. All these characteristics can provide a reference for the modeling of nickel–cadmium batteries.

Then, considering the characteristics of open-circuit voltage and polarized voltage and the complexity of the model, the equivalent circuit model of nickel–cadmium battery was constructed, in which the voltage hysteresis, ohmic polarization, electrochemical polarization, and concentration polarization were considered. Based on the HPPC experimental data, the average absolute error of the constructed model was only 4.05 mV, the root mean square error was only 7.40 mV, the maximum absolute error was 49.79 mV, and the relative error was less than 1% and the maximum relative error was less than 5% most of the time.

The SOC estimation method of nickel–cadmium battery based on the established dynamic model and the AUKF algorithm was proposed. According to the estimated results from the measured data, it can be seen that, although the method is insensitive to the initial value of SOC, it can converge to the real values even if the initial value has a 30% error. The average absolute error and root mean square error of the final SOC estimation results are less than 1%.

Author Contributions: Conceptualization, M.M.; methodology, Y.Z.; software, Y.H.; validation, Y.H.; formal analysis, Y.H.; investigation, Y.H.; resources, Y.H.; data curation, H.L.; writing—original draft preparation, M.M.; writing—review and editing, H.L.; visualization, H.L.; supervision, C.D.; project administration, C.D. All authors have read and agreed to the published version of the manuscript.

Data Availability Statement: The data presented in this study are available upon request from the corresponding author.

Conflicts of Interest: The authors declare no conflict of interest.

References

1. Xie, F.; Xu, J.; Liao, Q.; Zhang, Q.; Liu, B.; Shao, L.; Cai, J.; Shi, X.; Sun, Z.; Wong, C. Progress in niobium-based oxides as anode for fast-charging Li-ion batteries. *Energy Rev.* **2023**, *2*, 100027. [CrossRef]
2. Wang, S.; Zhu, Y.; Xu, X.; Shao, Z.; Sunarso, J. Adsorption-based synthesis of Co_3O_4/C composite anode for high performance lithium-ion batteries. *Energy* **2017**, *125*, 569–575. [CrossRef]
3. Mu, X.; Liu, Y.; Zhang, W. Study on application of new energy technology on railway vehicles. *Smart Rail Transit* **2021**, *58*, 29–35.
4. Long, Y. Review of auxiliary power supply batteries systems for railway applications. *Chin. Battery Ind.* **2021**, *25*, 221–226.
5. Wang, Q.; Zhao, L.; Yu, X. Comparative analysis of electric vehicle BMS related standards based on SOC estimation accuracy experiments. *Qual. Certif.* **2022**, *16*, 75–76.
6. Liu, Z.; Dang, X.; Jing, B. A novel model-based state of charge estimation for lithium-ion battery using adaptive robust iterative cubature Kalman filter. *Electr. Power Syst. Res.* **2019**, *177*, 105951.1–105951.11. [CrossRef]
7. Gao, M.; Xu, H.; Wu, M. Review of SOC estimation methods for power battery based on equivalent circuit model. *J. Electr. Eng.* **2021**, *16*, 90–102.
8. Zhang, S.; Guo, X.; Dou, X. A data-driven coulomb counting method for state of charge calibration and estimation of lithium-ion battery. *Sustain. Energy Technol. Assess.* **2020**, *40*, 100752.1–100752.15. [CrossRef]
9. Wu, C. Review of state of charge estimation for power battery. *Chin. J. Power Sources* **2017**, *41*, 1795–1798.
10. Zhang, Z.; Guo, T.; Gao, M. Review of SoCestimation methods for electric vehicle li-ion batteries. *J. Electron. Inf. Technol.* **2021**, *43*, 1803–1815.
11. Shrivastava, P.; Soon, T.K.; Idris, M.Y.I.B. Overview of model-based online state-of-charge estimation using Kalman filter family for lithium-ion batteries. *Renew. Sustain. Energy Rev.* **2019**, *113*, 109233.01–109233.23. [CrossRef]

12. Wu, L.; Pang, H.; Jin, J. A review of SOC estimation methods for lithium-ion batteries based on electrochemical model. *Trans. China Electrotech. Soc.* **2022**, *37*, 1703–1725.
13. Zhang, H.; Yun, F.; Shen, X. Research progress on thermal model of lithium ion battery. *Chin. J. Nonferrous Met.* **2023**, *33*, 817–828.
14. Zheng, X.; Guo, F. Overview of power battery model. *Chin. J. Power Sources* **2019**, *43*, 521–524.
15. Feng, F. Research on State of Charge Estimation and Equalization Strategy of Lithium Battery in Electric Vehicle Used in Cold Area. Ph.D. Thesis, Harbin Institute of Technology, Harbin, China, 2017.
16. He, Z.; Yang, G.; Lu, L. A modeling method for power battery dynamics. *Trans. China Electrotech. Soc.* **2016**, *31*, 194–203.
17. Zhuang, Q.; Yang, Z.; Zhang, L. Research progress on diagnosis of electrochemical impedance spectroscopy in lithium-ion batteries. *Prog. Chem.* **2020**, *32*, 761–791.
18. Lai, X.; Li, Y.; Zheng, Y. An overall estimation of state-of-charge based on SOC-OCV optimization curve and EKF for lithium-ion battery. *Automot. Eng.* **2021**, *43*, 19–26.
19. Guo, B.; Zhang, P.; Wang, W. Research on SOC estimation of LiFePO$_4$ battery based on OCV-SOC curve cluster. *Chin. J. Power Sources* **2019**, *43*, 1125–1128.
20. Lavigne, L.; Sabatier, J.; Francisco, J.M. Lithium-ion open circuit voltage (OCV) curve modelling and its ageing adjustment. *J. Power Sources* **2016**, *324*, 694–703. [CrossRef]
21. Garcia-Plaza, M.; Serrano-Jiménez, D.; Carrasco, J.E.G. A Ni–Cd battery model considering state of charge and hysteresis effects. *J. Power Sources* **2015**, *275*, 595–604. [CrossRef]
22. Sunil, K.; Pradhan, B. Battery management strategies: An essential review for battery state of health monitoring techniques. *J. Energy Storage* **2022**, *51*, 104427.
23. Afandi, A.; Sumantri, B.; Windarko, N.A. Estimation state of charge (SOC) of Ultracapacitor based on classical equivalent circuit using Extended Kalman Filter. In Proceedings of the 2020 International Electronics Symposium (IES), Nanjing, China, 8–10 November 2019; pp. 31–36.
24. Aung, H.; Low, K.S. Temperature dependent state-of-charge estimation of lithium ion battery using dual spherical unscented Kalman filter. *IET Power Electron.* **2015**, *8*, 2026–2033. [CrossRef]
25. Nguyen, T.T.; Khan, A.B.; Ko, Y. An accurate state of charge estimation method for lithium iron phosphate battery using a combination of an unscented Kalman filter and a particle filter. *Energies* **2020**, *13*, 4536. [CrossRef]
26. Xiao, L.; Wang, S.; Chang, L. Attitude determination for satellite using adaptive unscented Kalman filter. *Opt. Precis. Eng.* **2021**, *29*, 637–645. [CrossRef]
27. Xie, F.; Wang, S.; James, C. A novel intelligent SOC prediction method of lithium-ion battery packs based on the improved unscented transformation. *IOP Conf. Ser. Earth Environ. Sci.* **2019**, *227*, 032034. [CrossRef]
28. Wang, C.; Li, Q. State of charge estimation of ultracapacitors based on unscented Kalman filter. *Chin. J. Power Sources* **2021**, *45*, 1624–1627.
29. Xiang, L.; Cai, L.; Dai, N. State of charge estimation of lithium-ion batteries based on an improved Sage-Husa extended Kalman filter algorithm. *World Electr. Veh. J.* **2022**, *13*, 220. [CrossRef]
30. Wang, X.; Wang, A.; Wang, D. A modified Sage-Husa adaptive Kalman filter for state estimation of electric vehicle servo control system. *Energy Rep.* **2022**, *8*, 20–27. [CrossRef]
31. Chen, J.; Zhou, J.; Gong, D. The application of the modified Sage-Husa adaptive Kalman filter in the excitation force identification of under-chassis active equipment for railway vehicles. *J. Vib. Acoust.* **2021**, *143*, 031009.1–031009.8. [CrossRef]
32. Li, X.; Sun, L.; Ma, Y. Energy state estimation of lithium-ion batteries based on sage-husa EKF algorithm. *Energy Storage Sci. Technol.* **2022**, *11*, 3603–3612.
33. Dong, X.; Wu, P.; Ge, C. State of charge estimation of Li-ion battery based on adaptive unscented Kalman filter. *Adv. Technol. Electr. Eng. Energy* **2021**, *40*, 58–65.